

# Single- and double-slit collimating effects on fast-atom diffraction spectra.

M.S. Gravielle<sup>1</sup> and J.E. Miraglia<sup>1</sup>

<sup>1</sup>*Instituto de Astronomía y Física del Espacio (IAFE, CONICET-UBA),  
casilla de correo 67, sucursal 28, C1428EGA, Buenos Aires, Argentina.*

(Dated: May 10, 2022)

Diffraction patterns produced by swift He atoms grazingly impinging on a LiF(001) surface are investigated focusing on the influence of the beam collimation. Single- and double-slit collimating devices situated in front of the beam source are considered. To describe the scattering process we use the Surface Initial Value Representation (SIVR) approximation, which is a semi-quantum approach that incorporates a realistic description of the initial wave packet in terms of the collimating parameters. For a single-slit collimation, the width of the collimating aperture controls the shape of the azimuthal angle distribution, making different interference mechanisms visible, while the length of the slit affects the polar angle distribution. Additionally, we found that by means of a double-slit collimation it might be possible to obtain a wide polar angle distribution, which is associated with a large spread of the initial momentum perpendicular to the surface, derived from the uncertainty principle. It might be used as a simple way to probe the surface potential for different normal distances.

PACS numbers: 34.35.+a, 79.20.Rf, 37.25.+k

## I. INTRODUCTION

In the last time grazing-incidence fast atom diffraction (GIFAD or FAD) [1, 2] has emerged as a powerful surface analysis technique that allows one to inspect ordered surfaces, providing detailed information on their morphological and electronic characteristics [3–5]. The extreme sensitivity of FAD patterns to the projectile-surface interaction relies on the preservation of quantum coherence [6–9], and in this aspect the collimating conditions of the incident beam play an important role. In particular, recent experimental [10] and theoretical [11] works have shown that FAD patterns are strongly affected by the width of the collimating aperture, which determines that two different mechanisms - Bragg diffraction or supernumerary rainbows - can be alternatively observed.

In this article we theoretically investigate the influence of beam collimation on FAD spectra by considering not only a single-slit but also a double-slit collimating device. In the model, the transversal *coherence* size of the initial wave packet associated with the incident particle is determined from the collimating conditions by means of the Van Cittert-Zernike theorem [12], while the elastic atom-surface scattering is described within a recently developed semi-quantum approach, named Surface-Initial Value Representation (SIVR) approximation [13]. The SIVR method offers a clear representation of the main mechanisms of the process in terms of classical trajectories through the Feynman path integral formulation of quantum mechanics [14]. It includes an approximate description of classically forbidden transitions on the dark side of the rainbow angle, giving a successful representation of the experimental FAD patterns over the whole angular range [11, 13], without requiring the use of convolutions to smooth the theoretical curves [15].

The SIVR approximation is here applied to evaluate FAD patterns for He atoms grazingly impinging on a

LiF(001) surface after going through a collimating aperture formed by one or two parallel slits. The size and separation of such slits, which limit the effective size of the extended incoherent beam source, determine the aspect of FAD patterns, making different interference mechanisms visible. The paper is organized as follows. The theoretical formalism is summarized in Sec. II. Results for different sizes of the collimating apertures are presented and discussed in Sec. III, while in Sec. IV we outline our conclusions. Atomic units (a.u.) are used unless otherwise stated.

## II. THEORETICAL MODEL

We consider an atomic projectile ( $P$ ), with initial momentum  $\vec{K}_i$ , which is elastically scattered from a crystal surface ( $S$ ), ending in a final state with momentum  $\vec{K}_f$  and total energy  $E = K_f^2/(2m_P) = K_i^2/(2m_P)$ ,  $m_P$  being the projectile mass. The frame of reference is located on the first atomic layer, with the surface contained in the  $x-y$  plane, the  $\hat{x}$  versor along the incidence direction and the  $\hat{z}$  versor oriented perpendicular to the surface, aiming towards the vacuum region (see Fig. 1).

Within the SIVR approximation [13], the amplitude per unit of surface area  $\mathcal{S}$  for the transition  $\vec{K}_i \rightarrow \vec{K}_f$  reads

$$A_{if}^{(SIVR)} = \frac{1}{\mathcal{S}} \int_S d\vec{R}_o f_i(\vec{R}_o) \int d\vec{K}_o g_i(\vec{K}_o) \times a_{if}^{(SIVR)}(\vec{R}_o, \vec{K}_o), \quad (1)$$

where  $a_{if}^{(SIVR)}(\vec{R}_o, \vec{K}_o)$  is the partial transition amplitude associated with the classical projectile path  $\vec{\mathcal{R}}_t \equiv \vec{\mathcal{R}}_t(\vec{R}_o, \vec{K}_o)$ , with  $\vec{R}_o$  and  $\vec{K}_o$  being the starting position and momentum, respectively, at the time  $t = 0$ . The

functions  $f_i(\vec{R}_o)$  and  $g_i(\vec{K}_o)$  describe the profiles of the position and momentum distributions of the initial wave packet, which depend on the beam collimation.

In Eq. (1) the starting position can be expressed as  $\vec{R}_o = \vec{R}_{os} + Z_o \hat{z}$ , where  $\vec{R}_{os} = X_o \hat{x} + Y_o \hat{y}$  is the component parallel to the surface plane and  $Z_o$  is a fixed distance, here chosen as equal to the lattice constant, for which the projectile is hardly affected by the surface interaction. The partial transition amplitude  $a_{if}^{(SIVR)}$  reads

$$a_{if}^{(SIVR)}(\vec{R}_o, \vec{K}_o) = - \int_0^{+\infty} dt \frac{|J_M(t)|^{1/2} e^{i\nu_t \pi/2}}{(2\pi i)^{9/2}} V_{SP}(\vec{R}_t) \times \exp \left[ i \left( \varphi_t^{(SIVR)} - \vec{Q} \cdot \vec{R}_o \right) \right] \quad (2)$$

where  $V_{SP}$  represents the the surface-projectile interaction,  $\vec{Q} = \vec{K}_f - \vec{K}_i$  is the projectile momentum transfer, and

$$\varphi_t^{(SIVR)} = \int_0^t dt' \left[ \frac{1}{2m_P} \left( \vec{K}_f - \vec{P}_{t'} \right)^2 - V_{SP}(\vec{R}_{t'}) \right] \quad (3)$$

is the SIVR phase at the time  $t$ , with  $\vec{P}_t = m_P d\vec{R}_t/dt$  the classical projectile momentum. In Eq. (2) the Maslov function [16]

$$J_M(t) = \det \left[ \frac{\partial \vec{R}_t(\vec{R}_o, \vec{K}_o)}{\partial \vec{K}_o} \right] = |J_M(t)| \exp(i\nu_t \pi) \quad (4)$$

is a Jacobian factor (a determinant) evaluated along the classical trajectory  $\vec{R}_t$ , with  $|J_M(t)|$  the modulus of  $J_M(t)$  and  $\nu_t$  an integer number that accounts for the sign of  $J_M(t)$  at a given time  $t$ , satisfying that every time that  $J_M(t)$  changes its sign along the trajectory,  $\nu_t$  increases by 1.

In this work we consider a collimating device formed by  $n$  equivalent rectangular apertures (with  $n = 1$  or 2) placed just in front of an extended incoherent beam source, at a long distance  $L$  from the surface. Each of the rectangular openings is oriented in such a way that the corresponding transversal width,  $d_y$ , is parallel to the surface (i.e. parallel to the  $\hat{y}$  versor), while the side of length  $d_x$  forms an angle  $\theta_x = \pi/2 - \theta_i$  with the surface (i.e. with the  $\hat{x}$  versor), with  $\theta_i$  being the glancing incidence angle, as depicted in Fig. 1. We assume that the spatial profile of the coherent initial wave packet at a distance  $Z_o$  from the surface is determined by the the complex grade of coherence  $\mu_n(X_o, Y_o)$  as given by the Van Cittert-Zernike theorem [12], reading

$$|\mu_n(X_o, Y_o)|^2 = j_0^2\left(\frac{\pi d_x}{\lambda_{\perp} L} X_o\right) j_0^2\left(\frac{\pi d_y}{\lambda L} Y_o\right) \times \cos^2\left((n-1) \frac{\pi b}{\lambda_{\perp} L} X_o\right), \quad (5)$$

where  $n = 1, 2$ , represents the number of collimating openings,  $b$  is the distance between the centers of the

apertures, and  $j_0(x)$  is the spherical Bessel function. The de Broglie wavelengths  $\lambda$  and  $\lambda_{\perp}$  are defined as

$$\lambda = 2\pi/K_i, \text{ and } \lambda_{\perp} = \lambda/\sin \theta_i, \quad (6)$$

respectively, this last one being associated with the initial motion normal to the surface plane.

For small  $X_o$  and  $Y_o$  values, the spatial profile of the initial wave packet  $|f_i(\vec{R}_{os})|^2 \simeq |\mu_n(X_o, Y_o)|^2$  can be approximated as a product of Gaussian functions,  $G(\omega, x) = [2/(\pi\omega^2)]^{1/4} \exp(-x^2/\omega^2)$ , as

$$f_i(\vec{R}_{os}) = G(\sigma_x, X_o) G(\sigma_y, Y_o), \quad (7)$$

where the parameters  $\sigma_x$  and  $\sigma_y$  determine the *transversal coherence size* of the initial wave packet [17], reading

$$\sigma_x = \frac{\lambda_{\perp}}{\sqrt{2}} \frac{L}{D_x(n)}, \quad \sigma_y = \frac{\lambda}{\sqrt{2}} \frac{L}{d_y}, \quad (8)$$

with  $D_x(1) = d_x$  for a single-slit collimator and  $D_x(2) = b$  for a double-slit one.

Concerning the starting momentum  $\vec{K}_o$ , since we are dealing with an incident beam with a well defined energy, i.e.,  $\Delta E/E \ll 1$  [10], it satisfies energy conservation, with  $K_0 = |\vec{K}_0| = \sqrt{2m_P E}$ . Therefore, the momentum profile of the initial wave packet,  $g_i(\vec{K}_o)$ , can be replaced by the angular profile

$$g_i(\vec{K}_o) \simeq g_i(\Omega_o) = G(\sigma_{\theta}, \theta_o - \theta_i) G(\sigma_{\varphi}, \varphi_o), \quad (9)$$

where  $\Omega_o \equiv (\theta_o, \varphi_o)$  is the solid angle corresponding to the  $\vec{K}_o$  direction. The angular widths of the  $\theta_o$ - and  $\varphi_o$ -distributions are derived from Eq. (7) by applying the Heisenberg uncertainty relation [18], reading

$$\sigma_{\theta} = \frac{\lambda_{\perp}}{2\sigma_x}, \text{ and } \sigma_{\varphi} = \frac{\lambda}{2\sigma_y}, \quad (10)$$

respectively.

Finally, by replacing Eqs. (7) and (9) in Eq. (1), the SIVR transition amplitude can be expressed as

$$A_{if}^{(SIVR)} = \frac{m_P K_i}{S} \int_S d\vec{R}_{os} f_i(\vec{R}_{os}) \int d\Omega_o g_i(\Omega_o) \times a_{if}^{(SIVR)}(\vec{R}_o, \vec{K}_o), \quad (11)$$

where  $a_{if}^{(SIVR)}$  is given by Eq. (2). Details of the derivation of the SIVR method are given in Refs. [11, 13].

### III. RESULTS

With the aim of studying the dependence of FAD patterns on the collimation conditions we apply the SIVR method to 1 keV  $^4\text{He}$  atoms impinging on a LiF(001) surface along the  $\langle 110 \rangle$  channel, with the incidence angle

$\theta_i = 0.99$  deg. For this collision system, experimental results obtained by using a single collimating aperture with different widths were reported in Ref. [10].

In this section, results for single-slit and double-slit collimating devices situated in front of an extended incoherent beam source, at a distance  $L = 25$  cm from the surface [10], will be separately analyzed. The SIVR differential probability for elastic scattering with final momentum  $\vec{K}_f$  in the direction of the solid angle  $\Omega_f \equiv (\theta_f, \varphi_f)$  was derived from Eq. (11) as [13]

$$dP^{(SIVR)}/d\Omega_f = K_f^2 \left| A_{if}^{(SIVR)} \right|^2, \quad (12)$$

with  $\theta_f$  being the final polar angle, measured with respect to the surface, and  $\varphi_f$  being the azimuthal angle, measured with respect to the  $\hat{x}$  axis (Fig. 1). The transition amplitude  $A_{if}^{(SIVR)}$  was obtained from Eq. (11) by employing the MonteCarlo technique with more than  $4 \times 10^5$  points in the  $\vec{R}_{os}$ - and  $\Omega_o$ - integrations. Like in Refs. [11, 13], the projectile-surface interaction was evaluated with a pairwise additive potential that includes no local terms of the electronic density in the kinetic and exchange contributions, as well as projectile polarization and rumpling effects.

#### A. Single collimating slit

We start analyzing the influence of the width of a single collimating aperture,  $d_y$ , which determines the effective length of the extended beam source in the direction transversal to the incidence channel. In Fig. 2 we show two-dimensional projectile distributions, as a function of  $\theta_f$  and  $\varphi_f$ , derived within the SIVR approximation by considering single collimating slits with the same length -  $d_x = 1.5$  mm - but different  $d_y$ . For the narrowest aperture -  $d_y = 0.1$  mm - the final angular distribution presents thin peaks associated with Bragg diffraction, which are situated at azimuthal angles that verify [19]

$$\sin \varphi_f = m\lambda/a_y, \quad (13)$$

where  $m$  is an integer number that determines the Bragg order and  $a_y$  is the length of the reduced unit cell along the  $\hat{y}$  direction. From Fig. 2 we observe that the width of these Bragg peaks notoriously increases as  $d_y$  augments. In particular, for  $d_y = 0.6$  mm, Bragg interference is almost completely blurred out and intense rainbow maxima at the outermost azimuthal angles of the angular spectrum arise [20]. For wider collimating apertures, i.e.,  $d_y \gtrsim 0.8$  mm, Bragg peaks vanish, giving rise to supernumerary rainbow structures in the final projectile distribution. As discussed in Refs. [10, 11], this behavior is associated with the transversal length  $\mathcal{D}_y$  of the area  $\mathcal{S}$  of the surface plane that is coherently illuminated by the incident beam. The transversal length of the coherently illuminated region can be estimated from Eq.

(5) as  $\mathcal{D}_y = 2\sqrt{2}\sigma_y$  [11], being inversely proportional to  $d_y$ , as given by Eq. (8). Hence, for the narrower collimating apertures of Fig. 2 several reduced unit cells in the direction transversal to the incidence channel become coherently illuminated by the initial wave packet, originating sharp Bragg maxima. But when the width of the collimating opening augments, the number of reduced unit cells that are coherently lighted decreases, and for  $d_y \gtrsim 0.8$  mm only one reduced unit cell is coherently illuminated along the  $\hat{y}$  direction. Consequently, interferences coming from different parallel channels, which are associated with the Bragg mechanism [19, 21], disappear and the unit-cell form factor corresponding to the interference inside one channel governs the projectile distribution [21], causing supernumerary rainbow structures to be visible instead [22].

Such an effect of the width of the collimating aperture on FAD patterns was also experimentally found in Ref. [10]. In Fig. 3, SIVR diffraction spectra for two different collimating widths -  $d_y = 0.2$  mm and  $d_y = 1.0$  mm - are compared with the corresponding experimental data extracted from Ref. [10], showing a very good agreement [11]. For the narrowest aperture (left column), the experimental and theoretical distributions present well-defined Bragg peaks laying on a thick annulus, whose mean radius is approximately equal to  $\theta_i$ . However, these interference structures completely disappear when the width of the opening increases, as it happens in the panels of the right column, where only maxima at the rainbow deflection angles  $\pm\Theta_{rb}$  are clearly observed.

In the case of a single collimating slit, the thickness of the annulus corresponding to the  $(\theta_f, \varphi_f)$  distribution of scattered projectiles is controlled by the length of the collimating aperture, increasing as  $D_x(1) = d_x$  augments. In Fig. 4 we show angular projectile distributions derived from the SIVR approach by considering single collimating slits with the same width -  $d_y = 0.2$  mm - and different lengths. For the small square aperture of Fig. 4 (a), with  $d_x = d_y = 0.2$  mm, the Bragg peaks look like circular spots lying on a thin ring whose radius is equal to  $\theta_i$ . But the thickness of this ring augments as  $d_x$  increases, and for  $d_x = 0.5$  mm (Fig. 4 (b)) the spots become slightly elongated strips. For longer collimating apertures, with  $d_x \gtrsim 1.5$  mm, not only the length of the interference fringes augments but also the different Bragg orders are situated at different radius, displaying additional interference structures along the  $\theta_f$ - axis. This effect is related to the  $\theta_o$ - spread of the initial wave packet, which is determined by  $\sigma_\theta$ , being proportional to  $d_x$  as given by Eqs. (10) and (8). Large  $d_x$  values produce a wide spread of the impact momentum normal to the surface plane,  $|K_{oz}| = K_o \sin \theta_o$ , originating interference structures similar to those observed in the diffraction charts for different normal energies  $E_\perp = E \sin^2 \theta_i$ . Then, the intensity oscillations along the  $\theta_f$ - axis observed for long collimating openings are exploring the surface potential for different distances to the topmost atomic plane.

## B. Double collimating slit

In the case of a double collimating slit, the length of the coherently illuminated region along the incidence channel is determined by  $D_x(2) = b$ , as given by Eq. (8). Therefore, under similar collimating conditions a double-slit collimating device produces a larger  $\theta_o$ -dispersion than the one corresponding to a single slit. Since a wide  $\theta_o$ -spread leads to a large dispersion of the perpendicular momentum  $K_{oz}$ , the angular projectile distributions derived by using a double aperture with a separation  $b$  of a few millimeters show unequivocal interference structures in the final polar angle axis, as observed in Fig. 5. In particular, the angular distribution for  $b = 5.0$  mm resembles the usual diffraction chart, which is obtained with a single-slit collimator by varying the incidence angle  $\theta_i$ , or what is the same, the normal energy  $E_\perp$ , to cover the whole perpendicular energy spectrum. In Fig. 6 we compare the SIVR angular spectrum derived by using a double-slit collimating device with  $b = 5.0$  mm with the diffraction chart obtained from the SIVR approach with a single slit, both collimating apertures with the same size:  $d_x = d_y = 0.2$  mm. The similarities between the projectile distributions of Figs. 6 (a) and 6 (b) are evident, reinforcing the idea that double collimating slits might be employed to probe potential energy surfaces corresponding to different normal energies, instead of the commonly used diffraction charts.

Lastly, notice that any change in the present collimation setups might affect our results and it should be specifically investigated. Moreover, we have considered fixed incidence conditions, i.e., constant de Broglie wavelengths. However, the spatial spread of the initial wave packet depends on  $\lambda$  and  $\lambda_\perp$ , as given by Eq. (8). Then, a variation of the incidence energy or angle would modify such a spread, affecting the shape of the diffraction patterns.

## IV. CONCLUSIONS

We have investigated the effect of the collimation of the incident beam on FAD patterns by considering a single-

and a double-slit collimator that limits the effective size of an extended incoherent atom source. Projectile distributions originated by elastic scattering were derived from the SIVR approximation [13] by incorporating a realistic description of the coherent initial wave packet in terms of the collimating parameters. The model was applied to helium atoms grazingly impinging on a LiF(001) surface, considering a fixed incidence condition and different sizes of the rectangular collimating apertures. For a single-slit collimator, the SIVR interference patterns are strongly affected by the width of the collimating aperture, which makes Bragg peaks (supernumerary rainbows) visible for narrow (wide) apertures. In turn, the length of the collimating opening affects the polar angle distribution of scattered projectiles, producing additional interference structures in the  $\theta_f$ -axis for long collimating apertures. This effect is related to the dispersion of the normal momentum  $K_{oz}$  and it is more evident for a double-slit collimator.

In the case of a double-slit collimating device, the interference patterns along the final polar angle axis are governed by the separation between slits. By using separation distances between slits of several millimeters it would be possible to obtain projectile distributions covering a wide range of final polar angles. Such distributions might be used to probe the projectile-surface interaction for different normal distances, replacing the commonly used diffraction charts.

## Acknowledgments

The authors acknowledge financial support from CONICET, UBA, and ANPCyT of Argentina.

- 
- [1] A. Schüller, S. Wethekam, and H. Winter, *Phys. Rev. Lett.* **98** (2007) 016103.
  - [2] P. Rousseau, H. Khemliche, A.G. Borisov, and P. Roncin, *Phys. Rev. Lett.* **98** (2007) 016104.
  - [3] H. Winter and A. Schüller, *Prog. Surf. Sci.* **86** (2011) 169 and references therein.
  - [4] M. Debiossac *et al.*, *Phys. Rev. B* **90** (2014) 155308.
  - [5] A. Zugarramurdi *et al.*, *Appl. Phys. Lett.* **106** (2015) 101902.
  - [6] F. Aigner, N. Simonović, B. Solleder, L. Wirtz, and J. Burgdörfer, *Phys. Rev. Lett.* **101** (2008) 253201.
  - [7] J. Lienemann *et al.*, *Phys. Rev. Lett.* **106** (2011) 067602.
  - [8] N. Bundaleski, P. Soullisse, A. Momeni, H. Khemliche, and P. Roncin, *Nucl. Instrum. Meth. Phys. Res. B* **269** (2011) 1216.
  - [9] C. A. Ríos Rubiano, G.A. Bocan, J.I. Juaristi, and M.S. Gravielle, *Phys. Rev. A* **89** (2014) 032706.
  - [10] J. Seifert, J. Lienemann, A. Schüller, and H. Winter, *Nucl. Instrum. Meth. Phys. Res. B* **350** (2015) 99.
  - [11] M.S. Gravielle and J.E. Miraglia, *Phys. Rev. A* **92** (2015) 062709.
  - [12] M. Born and E. Wolf, *Principles of optics* (Pergamon

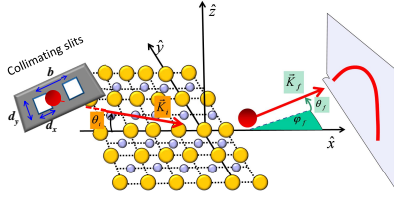


Fig. 1

FIG. 1: (Color online) Depiction of the FAD process, including the collimating device and the frame of reference.

Press, Oxford, 1986), chap. 10.

[13] M.S. Gravielle and J.E. Miraglia, Phys. Rev. A **90** (2014)

052718.

[14] W.H. Miller, J. Phys. Chem. A **105** (2001) 2942.

[15] C. A. Ríos Rubiano, G.A. Bocan, M.S. Gravielle, N. Bundaleski, H. Khemliche, and P. Roncin, Phys. Rev. A **87** (2013) 012903.

[16] R. Guantes, A.S. Sanz, J. Margalef-Roig, S. Miret-Artés, Surf. Sci. Rep. **53** (2004) 199, p. 213.

[17] A. Tonomura, *Progress in Optics* **23** (North-Holland, Amsterdam, 1986) 183.

[18] C. Cohen-Tannoudji, B. Diu, F.Laloë, *Quantum Mechanics* (Wiley-VCH, Paris, 2011), comp  $G_I$ .

[19] A. Schüller, and H. Winter, Nucl. Instrum. Meth. Phys. Res. B **267** (2009) 628.

[20] M.S. Gravielle and J.E. Miraglia, Phys. Rev. A **78** (2008) 022901.

[21] A. Schüller, H. Winter, M.S. Gravielle, J.M Pruneda, and J.E. Miraglia, Phys Rev. A **80** (2009) 062903.

[22] A. Schüller and H. Winter, Phys. Rev. Lett. **100** (2008) 097602.

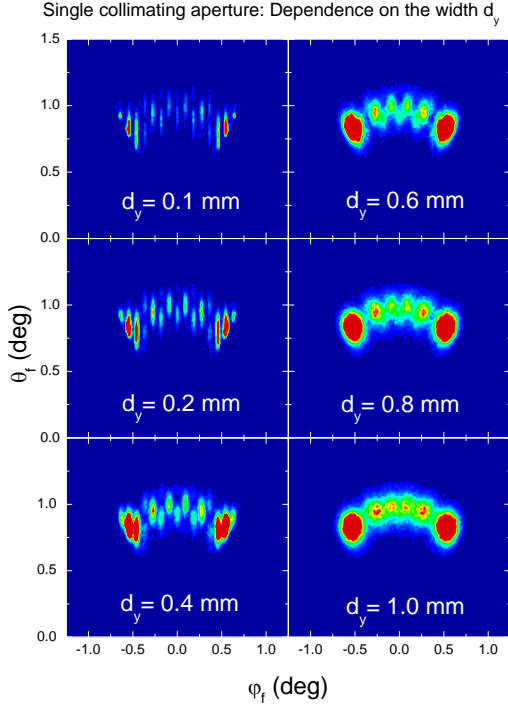


FIG. 2: (Color online) Two-dimensional projectile distribution, as a function of the final dispersion angles  $\theta_f$  and  $\varphi_f$ , for 1 keV  $^4\text{He}$  atoms impinging on LiF(001) along the  $\langle 110 \rangle$  direction with the incidence angle  $\theta_i = 0.99$  deg. The helium beam is collimated with a single rectangular aperture of length  $d_x = 1.5$  mm and different widths:  $d_y = 0.1, 0.2, 0.4, 0.6, 0.8$ , and  $1.0$  mm.

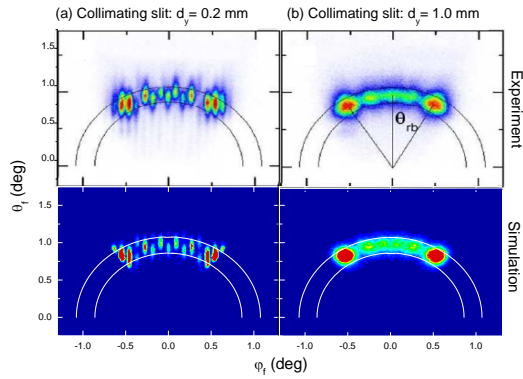


FIG. 3: (Color online) Similar to Fig. 2 for a single collimating aperture of length  $d_x = 1.5$  mm and two different widths: (a) (left column)  $d_y = 0.2$  mm; (b) (right column)  $d_y = 1.0$  mm. Upper panels, experimental distributions extracted from Ref. [10]; lower panels, our theoretical projectile distributions [11]. The radial lines in the right upper panel indicate the positions of the rainbow deflection angles  $\pm\Theta_{rb}$ .

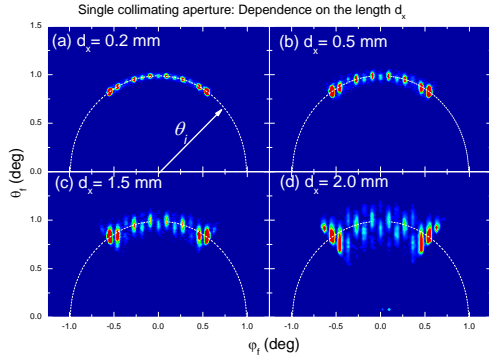


FIG. 4: (Color online) Similar to Fig. 2 for a single-slit collimating device of width  $d_y = 0.2$  mm and different lengths: (a)  $d_x = 0.2$  mm, (b)  $d_x = 0.5$  mm, (c)  $d_x = 1.5$  mm, and (d)  $d_x = 2.0$  mm. In all the panels: dashed line, circle of radius equal to the incidence angle  $\theta_i$ .

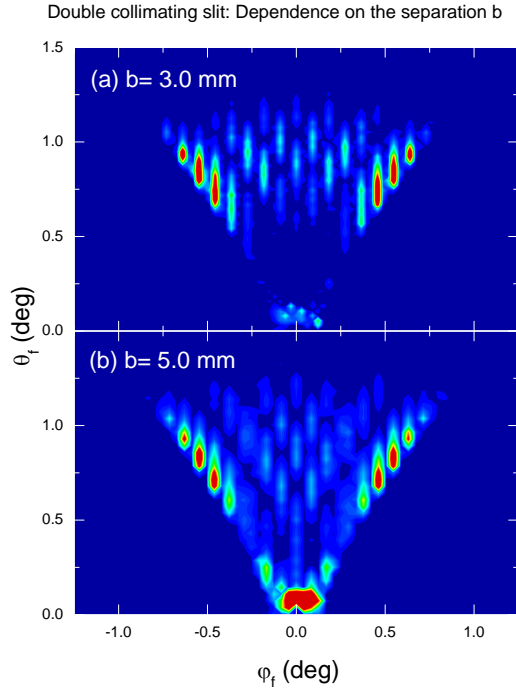


FIG. 5: (Color online) Similar to Fig. 2 for a double-slit collimating device, each of the apertures of size  $d_x = d_y = 0.2$  mm. The apertures are separated by a distance  $b$ , with: (a)  $b = 3.0$  mm, and (b)  $b = 5.0$  mm.

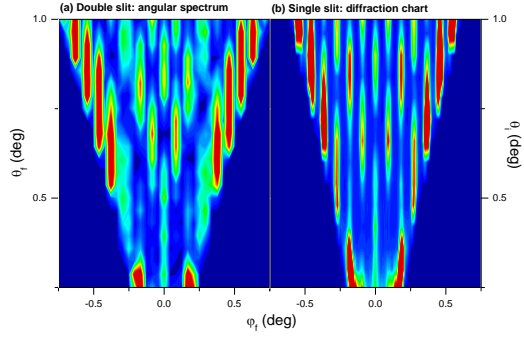


FIG. 6: (Color online) SIVR projectile distributions for 1 keV  $^4\text{He}$  atoms impinging on  $\text{LiF}(001)$  along the  $\langle 110 \rangle$  channel. (a) Angular distribution derived by considering the incidence angle  $\theta_i = 0.99$  deg and a double-slit collimating device with a separation  $b = 5.0$  mm. (b) Diffraction chart derived by considering different incidence angles  $\theta_i$  and a single-slit collimating device. Both collimating apertures of size  $d_x = d_y = 0.2$  mm.